Journal of Magnetic Resonance 305 (2019) 77–88

Contents lists available at ScienceDirect

Journal of Magnetic Resonance

journal homepage: www.elsevier.com/locate/jmr

TRASE 1D sequence performance in imperfect B_1 fields

Pallavi Bohidar [a], Hongwei Sun [b], Gordon E. Sarty [a], Jonathan C. Sharp [b,*]

[a] Space MRI Lab, Division of Biomedical Engineering, University of Saskatchewan, Saskatoon, Canada
[b] Department of Oncology, Faculty of Medicine & Dentistry, University of Alberta, Edmonton, Canada

ARTICLE INFO

Article history:
Received 9 May 2019
Revised 8 June 2019
Accepted 10 June 2019
Available online 13 June 2019

Keywords:
TRASE
MRI
B_1 inhomogeneity
Pulse sequence design
PSF

ABSTRACT

Transmit Array Spatial Encoding (TRASE) is an MRI technique that uses radio-frequency (RF) magnetic field (B_1) phase gradients for spatial encoding. A TRASE pulse sequence consists of a long echo train in which each echo samples a different *k*-space point. Due to the need for accurate refocusing, TRASE imaging performance depends on $|B_1|$ homogeneity. Although the CPMG echo train is often relied on to provide immunity against B_1 flip angle errors, this does not apply to TRASE echo trains. Due to the spatially dependent B_1 phases involved in TRASE imaging, the CPMG condition, where all spins flip about the y-axis in the rotating frame, can only be achieved at one single location within the sample. Moreover, CPMG only preserves one component of the transverse magnetization, the y-component, whereas TRASE requires both components to be retained. Here we investigate the performance of a set of variants of a 1-dimensional (1D) TRASE sequence under conditions of $|B_1|$ errors. We varied the B_1 transmit pulse RF waveform phases in an effort to optimize the TRASE imaging point spread function (PSF). The performance of 256 sequence variants, including those previously reported in the literature was studied. Both Bloch equation simulations and experimental confirmations were completed. Off-resonance (B_0 inhomogeneity) effects were not considered so that the effects of B_1 inhomogeneity alone could be understood. Results show that, using optimum transmit pulse phases, high quality image encoding is achievable over $\sim 90\%$ of the Nyquist field-of-view (FOV) for a practically realizable variation in B_1 amplitude ($\Delta|B_1| \leqslant \pm 11\%$). This improves significantly upon the performance of a previously-reported sequence which generated $\sim 75\%$ usable FOV within the Nyquist FOV.

1. Introduction

Conventional MRI technology uses rapidly switched B_0 gradients for spatial encoding. The B_0 gradient coils require complex electronics, water cooling systems, heavy power consumption and take up a significant amount of space [1]. Hence, conventional MRI instruments are unsuitable for use in remote locations such as space missions, rural areas, theatres of war, and medical field emergencies. For application in remote locations, portable, low-cost, and low-field MRI instruments are desirable. Such MRIs will be instrumental in studies aimed at monitoring astronaut health during space missions [2,3], for example, and will provide insight into similar physiological conditions observed on Earth [4].

Transmit Array Spatial Encoding (TRASE) is a novel imaging technique that uses transmit RF (B_1 field) phase gradients, instead of B_0 gradients, to encode spatial information [1,5]. This approach eliminates the use of B_0 gradient coils and the accompanying complex electronics. TRASE is a general *k*-space method, therefore, many analogues of standard MRI pulse sequences and experiments can be implemented in TRASE. Imaging in 2D and concepts for slice selection, using TRASE, have been reported [1,5,6]. TRASE has also been successfully implemented to obtain 2D in vivo MRI images [7,8]. Here 1D TRASE sequences were investigated. A 1D pulse sequence produces a 1D projection of a 3D object and this 1D image is termed the object profile.

The general problem addressed here is the performance of TRASE 1D sequence under an inhomogeneous $|B_1|$ field, which has not been previously reported in detail. The objective of the study was to investigate variants of a 1-dimensional TRASE sequence under conditions of $|B_1|$ inhomogeneity and/or calibration errors. The aim was to identify image artifacts that arise from B_1 errors and to understand their origin. We sought to select optimum B_1 transmit pulse phases to maximize the robustness against $|B_1|$ errors over the largest possible imaging volume. Although TRASE mandates the use of a specific sequence of B_1 phase gradients to traverse *k*-space, the choice of transmit pulse phases is open and so provides a degree of flexibility in sequence design. The choice of phases affects performance significantly, so we systematically investigated and characterized transmit pulse phase

---

* Corresponding author.
E-mail address: jcsharp@ualberta.ca (J.C. Sharp).

https://doi.org/10.1016/j.jmr.2019.06.005
1090-7807/

schemes, and searched for those schemes that generated echo trains for reliable TRASE imaging.

2. Theory

A 1D TRASE pulse sequence consists of an excitation pulse followed by a spin echo [9] train in which the refocusing pulses are alternately applied using two coils *A* and *B*. The B_1 fields from coils *A* and *B* are ideally of uniform magnitude but of different B_1 phase gradients. The effect of refocusing with alternating phase gradients induces a *k*-space evolution from one echo to the next, so that the sampling of an echo train yields a line of *k*-space. A 1D TRASE sequence of *N* echoes may be represented in terms of the coils used to apply the pulses as: $A-(AB)_{N/2}$. Fig. 1 demonstrates the concept of 1D TRASE *k*-space traversal, with B_1 encoding, using a $A-(AB)_{N/2}$ echo train. A TRASE 1D pulse sequence may be represented as follows:

$$(90)^A_{\phi_0} - \left[(\alpha)^A_{\phi_1} - e_1 - (\alpha)^B_{\phi_2} - e_2 - (\alpha)^A_{\phi_3} - e_3 - (\alpha)^B_{\phi_4} - e_4 - \right]_{N/4} \tag{1}$$

Here $(90)^A_{\phi_0}$ is the 90° excitation pulse with rotating frame phase ϕ_0 applied through transmit coil A; $\alpha^J_{\phi_n}$ is the n^{th} refocusing pulse with rotating frame phase ϕ_n and a flip angle of α applied through transmit coil '*J*' (A and B alternate for 1D TRASE); 'e_n' represents the echo collected after the n^{th} refocusing pulse; and *N* is the total number of echoes collected. In this study, all pulse sequences will be represented in terms of the refocusing pulse phases used i.e., $[\phi_1, \phi_2, \phi_3, \phi_4]$ with the excitation pulse always of zero phase $(\phi_0 = 0)$.

Expressing the component of the B_1 field in the transverse rotating frame as a complex number $B_1 = B_{1x} + iB_{1y}$, the RF field of the n^{th} transmit pulse for a general phase gradient coil, *J*, is

$$B_{1J}(\vec{r})_n = |B_{1J}|e^{i\left(\theta_J(\vec{r})+\phi_n\right)} \tag{2}$$

where $\theta_J(\vec{r}) = 2\pi\vec{k}_J \cdot \vec{r} = \vec{G}_J \cdot \vec{r}$ is the spatially-dependent B_1 phase for the coil $J \in \{A, B\}$ and ϕ_n is the phase of the applied RF waveform. The vector $\vec{r} = x\vec{i} + y\vec{j} + z\vec{k}$ represents a point in 3D space. Here $\vec{k}_J$, with units of cycles/meter, is the "*k*-space origin" of coil *J* and $\vec{G}_J = \nabla\theta_J(\vec{r})$ (ideally constant over $\vec{r}$) is the phase gradient with units radians/meter. For conventional RF coils, the coil *k*-space origin coincides with the center of *k*-space $(\vec{k}_J = \vec{G}_J = \vec{0})$. The variable $n, 0 \leqslant n \leqslant N$, represents the n^{th} transmit pulse for the TRASE pulse sequence collecting *N* echoes where the 0^{th} pulse is the 90° excitation pulse. Here the phase of the applied RF waveform ϕ_n is the B_1 phase seen by the spins at the coil center, such that

$$\phi_n = \psi_J + \theta_n \tag{3}$$

The term ψ_J is due to the geometric orientation of the coil *J* used to transmit the n^{th} pulse with console generated RF waveform phase θ_n. Consider a TRASE 1D setup with a uniform saddle coil having $\psi_A = 0°$ that is geometrically decoupled from a phase encoding twisted solenoid coil. The phase offset for the twisted solenoid will then be $\psi_B = 90°$. Since 1D notation takes the form: $\vec{r} = x\vec{i}, \vec{G}_J = G_J\vec{i}$ and $\vec{k}_J = k_J\vec{i}$, the B_1 field in Eq. (2) becomes a function of spatial position (x) such that $B_{1J}(x)_n = |B_{1J}|e^{i(\theta_J(x)+\phi_n)}$.

The spin-echo refocusing of a sample with a phase encoding coil encodes spatial information in the phase of the spins. The resulting transverse magnetization after the n^{th} refocusing pulse is expressed as a complex number $M_n(\vec{r}) = M_{x,n} + iM_{y,n}$. For an ideal n^{th}180° refocusing pulse, applied through coil *J*, the transverse magnetization $M_{n-1}(\vec{r})$ that exists before the pulse gets flipped 180° about the B_1 field direction, $\left(\theta_J(\vec{r}) + \phi_n\right)$ from Eq. (2), to $M_n(\vec{r})$, and is described by

$$M_n(\vec{r}) = M_{n-1}(\vec{r})^* e^{i2(\theta_J(\vec{r})+\phi_n)} \tag{4}$$

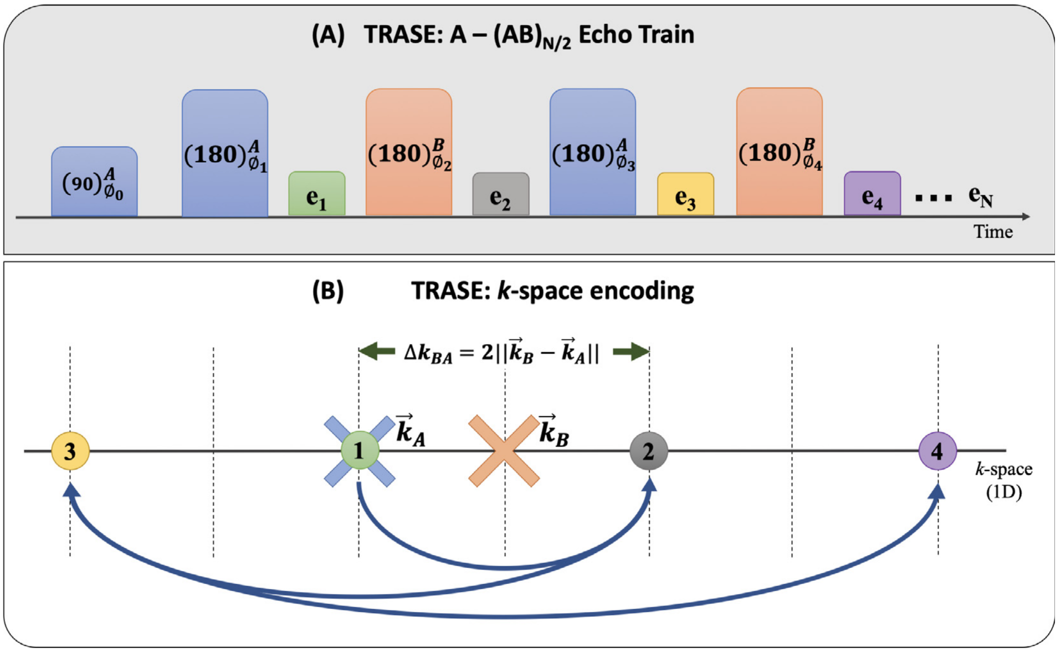

Fig. 1. TRASE 1D k-space encoding. (A) Echo train for a 1D TRASE experiment. A 90° excitation pulse is followed by a series of 180° refocusing pulses alternately applied with coils 'A' and 'B' which have transmit B_1 fields of uniform magnitude but different phase gradients. An echo is collected after each refocusing pulse. (B) The 1D *k*-space sampling pattern for the $A-(AB)_{N/2}$ echo train represented in panel (A). The color coded crosses represent the *k*-space coil origins and the color coded circles demonstrate the *k*-space traversal by the echo train. (For interpretation of the references to color in this figure legend, the reader is referred to the web version of this article.)

where $M_n(\vec{r})^* = M_{x,n} - iM_{y,n}$ is the complex conjugate of the transverse magnetization $M_n(\vec{r})$, and $\theta_J(\vec{r}) = \vec{G}_J \cdot \vec{r}$.

Based on Eq. (4), (assuming $\phi_n = 0$), the effect of the $n^{th}180^\circ$ refocusing pulse, for a given phase encoding coil J, is a reflection of the spin state about the coil k-space origin, $\vec{k}_J$, given by

$$\vec{k}_n = \vec{k}_J - (\vec{k}_{n-1} - \vec{k}_J) \quad \Rightarrow \quad \vec{k}_n = -\vec{k}_{n-1} + 2\vec{k}_J \tag{5}$$

where, $\vec{k}_{n-1}$ and $\vec{k}_n$ represent the k-space locations before and after the application of the $n^{th}180^\circ$ refocusing pulse respectively.

Since each echo in a TRASE experiment represents a point in k-space, TRASE is a k-space method equipped with the familiar Fourier transform based concepts of a Nyquist field-of-view (FOV) and spatial resolution. The number of echoes collected represent the extent of k-space covered. For an $A-(AB)_{N/2}$ echo train the FOV, V, is given by the reciprocal of the spacing between two consecutive k-space points:

$$V = \frac{1}{\Delta k_{BA}} = \frac{1}{2||\vec{k}_B - \vec{k}_A||} \tag{6}$$

This FOV, as given by Eq. (6), is also the distance between two points which experience identical phase increments. Consider two phase gradient coils $G_A = +1^\circ/\text{mm}$ and $G_B = -1^\circ/\text{mm}$. A pictorial representation of the FOV resulting from such a setup and the evolution of echo phases down the echo train for a few locations are shown in detail in Fig. 2.

The pixel separation in 1D (for un-zero filled FFT data), Δx, is then given by the reciprocal of the maximum k-space diameter (k_D) achieved by the sampling grid. For 'N' k-space points collected we have

$$\Delta x = \frac{1}{k_D} = \frac{1}{N(\Delta k)} = \frac{1}{N(2||\vec{k}_B - \vec{k}_A||)} = \frac{V}{N} \tag{7}$$

Some level of B_1 field inhomogeneity is inevitable for all practical transmit coil designs, with the potential to adversely affect performance. The TRASE imaging performance is reliant on accurate refocusing and depends on the $|B_1|$ homogeneity throughout the imaging volume. Additionally, as the use of two or more coils (B_1 phase gradients) is necessary for k-space traversal, alternating B_1 amplitudes may occur, due to different B_1 inhomogeneities and relative calibration errors between coils, with the potential to produce artifacts.

There is substantial literature addressing $|B_1|$ inhomogeneity using echo trains having different combinations of transmit pulse phases. Meiboom and Gill first proposed what is known as the Carr-Purcell-Meiboom-Gill (CMPG) [10] sequence:

$$(90)_0^A - \left[(180)_{90}^A - e_1 - (180)_{90}^A - e_2 - (180)_{90}^A - e_3 - (180)_{90}^A - e_4 - \right]_{N/4}$$

This $[90, 90, 90, 90]$ CPMG sequence modified the Carr-Purcell (CP) [11] sequence by introducing a 90° phase difference between the first excitation pulse and the following refocusing pulses. CPMG is insensitive to $|B_1|$ inhomogeneity in NMR and hence is widely applied to generate reliable echo trains in MRI experiments. However, Meiboom and Gill did not modify the echo train itself (all refocusing pulses still have identical phases). Later, Maudsley [12] proposed:

$$(90)_0^A - \left[(180)_{90}^A - e_1 - (180)_0^A - e_2 - (180)_{90}^A - e_3 - (180)_0^A - e_4 - \right]_{N/4}$$

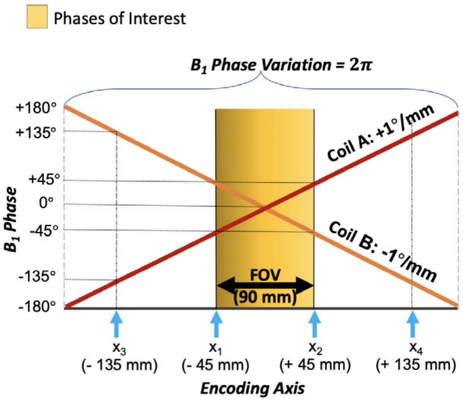

	-50 mm	-45 mm	-40 mm	-5 mm	0 mm	5 mm	40 mm	45 mm	50 mm
B_1 phase coil A	-50°	-45°	-40°	-5°	0°	+5°	+40°	+45°	+50°
B_1 phase coil B	+50°	+45°	+40°	+5°	0°	-5°	-40°	-45°	-50°
Echo 1 (e_1) phase	-140°	-135°	-130°	-95°	-90°	-85°	-50°	-45°	-40°
Echo 2 (e_2) phase	+240°	+225°	+210°	+105°	+90°	+75°	-30°	-45°	-60°
Echo 3 (e_3) phase	-340°	-315°	-290°	-115°	-90°	-65°	+110°	+135°	+160°
Echo 4 (e_4) phase	+440°	405°	+370°	+125°	+90°	+55°	-190°	-45°	-260°
Spin phase increment $e_1 \rightarrow e_3$	-200°	-180°	-160°	-20°	0°	+20°	+160°	+180°	+200°
Spin phase increment $e_2 \rightarrow e_4$	+200°	+180°	+160°	+20°	0°	-20°	-160°	-180°	-200°

Fig. 2. A depiction of the FOV resulting from a TRASE 1D setup with $G_A = +1^\circ/\text{mm}$ and $G_B = -1^\circ/\text{mm}$ using the sequence $(90)_0^A - \left[(180)_0^A - e_1 - (180)_0^B - e_2 - (180)_0^A - e_3 - (180)_0^B - e_4 - \right]_{N/4}$. A B_1 phase variation for both the coils which corresponds to a 90 mm spatial FOV is shown. The 'phases of interest' region depicts the subset of B_1 phases experienced throughout the FOV. The blue arrows on the spatial encoding axis represent locations that are either the edges of the FOV or get wrapped around as an edge. The B_1 phases down the echo train is shown for several sample locations to demonstrate how different locations experience different pulse sequences in TRASE. The spin phase evolution, recorded in tabular format, showcases how the phase increments (+180° and −180°) become identical at $x_1 = -45$ mm and $x_2 = 45$ mm. The same can be observed for points outside the FOV that experience aliasing, for example, $x = -50$ mm will get aliased as $x = 40$ mm (identical phase increments +160° and −200°). Although the B_1*phases* and *echo phases* at these aliased locations are different, the identical *phase increment* from one echo to the next renders the spatial encoding from the two locations indistinguishable and, as a result, gives rise to the aliasing effect. Therefore, only a subset of the whole range of B_1 phases generated by the phase gradient coil is relevant in a TRASE experiment. (For interpretation of the references to color in this figure legend, the reader is referred to the web version of this article.)

This [90, 0, 90, 0] sequence, referred as 'XY-4' in the literature [13], introduces a 90° phase difference between two successive refocusing pulses to compensate errors for both components of the transverse magnetization under conditions of $|B_1|$ inhomogeneity. CPMG only compensates one transverse component for $|B_1|$ errors and is therefore not well suited for TRASE echo trains which must generate and sustain the full phase information of the transverse magnetization. Levitt et al. [14] introduced "MLEV" sequences to study spin decoupling. MLEV sequences use iterative inversion pulses in the echo train and can be useful in minimizing the B_1 flip angle errors that propagate down the echo train [15]. A MLEV-4 sequence is represented as:

$$(90)_0^A - \left[(180)_0^A - e_1 - (180)_{180}^A - e_2 - (180)_0^A - e_3 - (180)_{180}^A - e_4 - \right]_{N/4}$$

Other refocusing pulse phase schemes, including MLEV [14] sequences, have been studied that compensate for both components of the transverse magnetization under conditions of $|B_1|$ inhomogeneity and/or B_1 amplitude errors [13,15–17]. All such pulse phase schemes are of potential interest to our study. However, the literature on echo trains is not directly applicable to TRASE for the following reason. In a TRASE experiment, the phase seen at a point in the sample, $\left(\theta_J(\overrightarrow{r}) + \phi_n\right)$ from Eq. (2), is a function of spatial position $\overrightarrow{r}$, due to the B_1 phase gradients involved. Therefore, different regions in the sample experience different B_1 phases, as shown in Fig. 2, and a TRASE experiment can be regarded as (from the point of view of the sample) not a single pulse sequence, but many. Any TRASE sequence will thus generate variants of itself across the FOV and the behaviour of such 'many-in-one' sequences under B_1 inhomogeneity is unstudied. Therefore, to search for an optimum TRASE technique, we must in effect probe an ensemble of pulse sequences simultaneously.

An alternating refocusing pulse phase scheme $[0, 0, 180, 180]$ was first reported in [1] but not investigated further. A recent simulation study [18] used composite transmit RF pulses to evaluate the performance of several refocusing pulse phase alternation schemes. Stockmann et al. [19] used swept Wideband Uniform-Rate Smooth truncation (WURST) RF pulses instead of hard pulses to mitigate the effects of B_0 inhomogeneity in TRASE imaging and studied a [90, 0, 90, 0] pulse sequence to create separate coherence pathways for conventional and spectral echoes. Although composite pulses [18] and swept pulses [19] may be useful in reducing TRASE's sensitivity to $|B_1|$ inhomogeneity, their longer duration relative to rectangular pulses impairs achievable spatial resolution. This is because an entire echo train in TRASE yields a line in k-space. Since T_2 decay of the sample reduces echo amplitude for high frequency k-space points, this imposes limitations on the total duration of the echo train. Therefore, for our application, the use of composite or swept pulses was deemed impractical. Some versions of alternate pulse schemes have been used in TRASE studies referenced earlier [1,18,19], but this approach to address $|B_1|$ inhomogeneity has not been systematically investigated.

3. Methods

3.1. Pulse Sequence Screening Simulation

A simulation based study was performed to screen the performance of different refocusing pulse phase schemes for 1D TRASE sequences, under conditions of $|B_1|$ inhomogeneity. A homogeneous B_0 field was assumed in all the simulations and only square refocusing pulses were considered, in order to minimize the echo train length. Sample relaxation effects were not considered in the simulations.

Bloch equation [20] simulations were performed using a FORTRAN based simulation program named "multibloch". Variants of 1D TRASE pulse sequences with 128 echoes (i.e. N = 128 in Eq. (1)) were investigated. The variants explored here were the different refocusing pulse phase combinations, represented as $[\phi_1, \phi_2, \phi_3, \phi_4]$. A maximum of 4 different refocusing pulse phases were used in cycled repetition down the echo train. Four different refocusing pulse phase values, ϕ_n, representing the principal axes of the transverse plane, i.e. $\phi_n \in \{0^\circ, 90^\circ, -90^\circ, 180^\circ\}$, were chosen with $4^4 = 256$ possible combinations. These 256 variants include in their number all the sequences discussed above in the literature review.

Each variant was numbered and represented as SXXX $[\phi_1, \phi_2, \phi_3, \phi_4]$, where XXX is a 3-digit numeric label (001-256). These were divided into 15 sub-groups, groups 1–15, based on the pattern of ϕ_n values used. The 15 sub-groups were further classified into 6 super-groups as shown in Table 1.

The simulations were performed for the following pulse sequence:

$$90_0^A - \left[160_{\phi_1}^A - e - 160_{\phi_2}^B - e - 160_{\phi_3}^A - e - 160_{\phi_4}^B - e - \right]_{128/4} \qquad (8)$$

Table 1

A list of the 6 super-groups and 15 sub-groups of 256 TRASE 1D pulse sequence variants based on the pattern of ϕ_n (applied refocusing pulse RF waveform phase) values.

Super Group	Sub Group	$[\phi_1, \phi_2, \phi_3, \phi_4]$ Pattern	SXXX	Variants	Notes
1.	1.	$[\gamma_1, \gamma_1, \gamma_1, \gamma_1]$	S001 - S004	4	1 phase value (includes CP [11] and CPMG [10])
2.	2.	$[\gamma_1, \gamma_2, \gamma_1, \gamma_2]$	S005 - S016	12	2 phase values, cycled with repetition,
	3.	$[\gamma_1, \gamma_1, \gamma_2, \gamma_2]$	S017 - S028	12	(includes XY-4 [12] & MLEV-4 [14])
3.	4.	$[\gamma_1, \gamma_2, \gamma_2, \gamma_1]$	S029 - S040	12	2 phase values (mirrored on repeat)
4.	5.	$[\gamma_1, \gamma_2, \gamma_2, \gamma_2]$	S041 - S052	12	
	6.	$[\gamma_1, \gamma_1, \gamma_1, \gamma_2]$	S053 - S064	12	2 phase values
	7.	$[\gamma_1, \gamma_2, \gamma_1, \gamma_1]$	S065 - S076	12	
	8.	$[\gamma_1, \gamma_1, \gamma_2, \gamma_1]$	S077 - S088	12	
5.	9.	$[\gamma_1, \gamma_1, \gamma_2, \gamma_3]$	S089 - S112	24	
	10.	$[\gamma_1, \gamma_2, \gamma_3, \gamma_3]$	S113 - S136	24	
	11.	$[\gamma_1, \gamma_2, \gamma_3, \gamma_1]$	S137 - S160	24	3 phase values
	12.	$[\gamma_1, \gamma_2, \gamma_1, \gamma_3]$	S161 - S184	24	
	13.	$[\gamma_1, \gamma_2, \gamma_2, \gamma_3]$	S185 - S208	24	
	14.	$[\gamma_1, \gamma_2, \gamma_3, \gamma_2]$	S209 - S232	24	
6.	15.	$[\gamma_1, \gamma_2, \gamma_3, \gamma_4]$	S233 - S256	24	4 phase values

Here the flip angle for the refocusing pulses was set to $\alpha_n = 160^\circ$ which is $\sim 11\%$ deviation from the ideal 180° flip angle and hence was deemed suitable for representing $|B_1|$ errors of a practical transmit coil. The simulations used B_1 phase gradients of $\pm 1^\circ$/mm which resulted in a Nyquist FOV of 90 mm i.e. ±45 mm (as described by Eq. (6) and Fig. 2). A pulse length of 100 µs for all the pulses in the sequence and an echo spacing of 2000 µs was used in all simulations.

The performance screening for all 256 variants of the pulse sequence was conducted in 3 stages. In *Stage 1*, using a 1D circular object profile of 50 mm diameter (simulated with 800 points corresponding to a discretization step size of 0.0626 mm), two scans were conducted for each of the 256 variants as follows: *Scan 1*- object was placed at the center of the FOV (−24 mm to +26 mm) and *Scan 2*- object was placed at one edge of the FOV with half of the object exceeding the FOV limit (+20 mm to +70 mm). This scheme of two scans per variant allowed the evaluation of the reconstructed object profiles over the entire FOV. To avoid the inadvertent masking of image artifacts due to symmetry, asymmetric object placement was used. Each variant was evaluated for its performance under $|B_1|$ errors by visually examining the reconstructed object profile throughout the FOV. The visual examination included comparing the obtained profile with ideal profiles (obtained from simulations using 180° refocusing pulses). The observations from the visual examination of this subset were further supported by computing the mean-squared-error (MSE), i.e. the variance (σ^2), between the obtained profile and the ideal profile in each scan (scans 1 and 2 as mentioned earlier). The evaluation criterion for this stage was the smoothness of object profiles and minimum variance. Smoothness here refers to the absence of ringing artifacts in the profile. The subset of variants which demonstrated a smooth object profile upon reconstruction passed *Stage 1* and were considered for *Stage 2* screening.

In *Stage 2*, another set of similar simulations were performed using the same sequence, but with five scans instead of the two scans used previously. A smaller 1D circular object of 30 mm diameter (simulated using 800 points corresponding to a discretization step size of 0.0375 mm) was placed across the FOV in five locations: −44 mm to −14 mm, −29 mm to +1 mm, −14 mm to +16 mm, +1 mm to +31 mm, and +16 mm to +46 mm. With these five scans in combination, the object profiles overlapped each other covering the entire FOV. In this stage, the evaluation criterion was again the smoothness of profile but with minimum artifacts.

In *Stage 3*, the members of the subset that passed the screening in *Stage 2* were evaluated for their performance under alternating $|B_1|$ errors (arising from the application of refocusing pulses down the echo train through alternating coils 'A' and 'B'). The objects used in *Stage 3* were similar to that of *Stage 1* but the flip angle errors were alternated for the refocusing pulses. The alternating refocusing pulses, between coils 'A' and 'B', were simulated with a maximum of 10° difference between their flip angles as representative a of real-life relative calibration error between two coils. The following pulse sequences were used to evaluate the variants in Stage 3:

$$90^A_0 - \left[155^A_{\phi_1} - e - 165^B_{\phi_2} - e - 155^A_{\phi_3} - e - 165^B_{\phi_4} - e-\right]_{128/4} \qquad (9)$$

$$90^A_0 - \left[195^A_{\phi_1} - e - 205^B_{\phi_2} - e - 195^A_{\phi_3} - e - 205^B_{\phi_4} - e-\right]_{128/4} \qquad (10)$$

The evaluation criterion here was the location of the artifacts in the profiles. In order to maximize the usable FOV, the variants generating artifacts at the center of the FOV were deemed unsuitable for further study. Of the variants that passed *Stage 3* and displayed identical performance, one variant was chosen to be studied in more detail (as described in the next section).

3.2. Point Spread Function (PSF) Simulation

The image reconstruction of a single point object represents an approximation of the point-spread function (PSF) in 1D for that location in a given MRI experiment. Since each location experiences different pulse phases, the TRASE PSF is not stationary, i.e. it is a function of position over the FOV. Each chosen variant, from *Stage 3* screening, was evaluated via its PSF at multiple locations across the 90 mm FOV for imperfect flip angle $\alpha^J_n = 160^\circ$. Relaxation effects ($T_1 = 1000$ ms and $T_2 = 100$ ms) were also included in PSF simulations to avoid FFT-based approximation errors when object placement occurred between pixels. A summarized list of all the simulation stages is described in Table 2.

3.3. Experiments

The simulations were followed by some experimental confirmations. TRASE 1D experiments were performed in an MRI system with a main magnetic field of $B_0 = 0.2$ T. A uniform saddle coil (coil 'A' with diameter 127 mm) geometrically decoupled from a phase gradient twisted solenoid coil (coil 'B' with diameter 156 mm), in combination, were used as transmit RF coils. This twisted solenoid coil design for generating a transmit B_1 field phase gradient in TRASE imaging has been reported in a recent study [21]. Coil 'B' provided a B_1 phase gradient of $\sim 6^\circ$/cm, ranging from −35° to +35° over a usable diameter of $\sim$ 120 mm for 1D TRASE imaging where a linear variation of B_1 phase was produced while the theoretical Nyquist FOV for this setup was 300 mm. Given these configurations, a cylindrical water phantom of $\sim$ 50 mm diameter was used to obtain its circular profile using TRASE 1D imaging. The object was placed nearly at the center of the imaging FOV in all experiments. With this experimental setup, 1D TRASE MRI experiments were conducted using the subset of variants that passed the *Stage 1* screening (8 variants). The TRASE 1D pulse sequence for all the experiments used pulses of length 200 µs with an echo spacing of 900 µs. The experimental results were compared with that of the simulations. The experimental results were further validated by performing simulations using the experimental parameters, with the same "multibloch" program, to match simulations with exact experimental conditions as closely as possible.

3.4. Reconstruction of TRASE data

The reconstruction routines used for both the simulation and experimental TRASE data employed the following steps:

1. *Echo phase corrections:* In order to use Eq. (4) to define accurate k-space locations (as in Eq. (5)) for TRASE reconstruction, it is necessary to remove the phase $\phi_n = \psi_J + \theta_n$ from each echo.

Table 2
A summarized list of the simulations performed for the TRASE 1D pulse sequence variants.

Simulation Stage	No. of Variants Considered
Screening Stage 1 Two scans over the FOV under 160° flip angle.	256
Screening Stage 2 Five scans covering the FOV under 160° flip angle.	8
Screening Stage 3 Two scans over the FOV under alternating flip angle errors.	4
Point-spread-function (PSF) evaluation	2

Therefore, each echo requires phase correction so that the console generated phases (θ_n) and the individual coil geometric phase offsets (ψ_J) do not disrupt the TRASE encoding ($\theta_J(\vec{r})$). In effect this process corrects the phase for the spins located at the coil center $x = 0$, so that all remaining phase is solely due to the phase gradients.

For the TRASE 1D pulse sequence in Eq. (1) the phase corrections ($-\beta_n$) were calculated as follows:

(a) The FID signal phase (β_0) after the $\pi/2$ excitation pulse is:

$$\beta_0 = \phi_0 + \pi/2 \tag{11}$$

(b) The phase of the first spin echo at the coil center is given by:

$$\beta_1 = -\beta_0 + 2\phi_1 \tag{12}$$

(c) After the first echo, each successive echo at the coil center ($\vec{0}$) then depends on the corresponding refocusing pulse phase and the phase of the previous echo as follows:

$$\beta_n = -\beta_{n-1} + 2\phi_n \tag{13}$$

The phase correction was then performed by applying the negative of this phase factor, $-\beta_n$, as calculated in Eq. (13), to each echo. This approach ensured that the B_1 phase encoding information due to $\theta_J(\vec{r})$ was retained while the phase offsets from transmit pulses and coil orientations were eliminated. Here the use of a simple receive coil with no phase gradient was assumed.

2. *Echo reordering:* As shown in Fig. 1 TRASE encoding collects k-space points alternately between the opposite halves of the k-space. Therefore it is necessary to reorder the even and odd numbered echoes (after phase corrections) before applying FFT techniques.
3. *FFT:* An FFT was applied to the phase corrected and reordered TRASE data to form the 1D images (object profiles) in simulations and experiments.

4. Results

4.1. Pulse Sequence Screening Simulations

The ideal reconstructed object profiles obtained by simulating a perfect B_1 field, (flip angle $\alpha_n = 180^\circ$) for simulation parameters $G_A = +1^\circ$/mm and $G_B = -1^\circ$/mm (90 mm theoretical FOV) are shown in Fig. 3. These ideal profiles served as a reference to visually examine the image artifacts and evaluate the performance of TRASE 1D sequences under $|B_1|$ errors. A brief summary of the *Stage 1* screening performance is shown in Fig. 4. The 256 variants investigated in *Stage 1* displayed a wide range of performance and some combinations of B_1 pulse phases generated significant image artifacts that made the object profiles unidentifiable. Based on visual examination of the image artifacts from *Stage 1* results, a subset of only eight variants (all belonging to super-group 2, sub-group 2), displayed identifiable object profiles are were considered for *Stage 2* screening, (results are shown in Fig. 5).

In the *Stage 2* screening, performance was evaluated on the basis of both identifiable object profiles and also artifacts. The variants showing ringing artifacts that contributed to uneven object profiles did not pass this screening stage. Four variants, out of the 8 considered, were found to exhibit object profiles with minimum artifacts (no ringing) under B_1 errors (see Fig. 6). These four variants that passed the *Stage 2* screening are listed in Table 3. The *Stage 1* performance of these four variants in comparison with S002[90, 90, 90, 90] CPMG is shown in Table 4. (See Fig. 8 for CPMG simulation results.) This table demonstrates the usable FOV, evaluated from visual inspection of the image artifacts, and the variance σ^2 (MSEs) from ideal profiles (for *Stage 1* scans 1 and 2). The usable FOV is a percentage of the theoretical FOV generated where image artifacts are absent. All these four pulse sequences belong to the super-group 2, sub-group 2 - $\beta_1\beta_2\beta_1\beta_2$ pattern (see Table 1). The data in this table show that the variance (σ^2) for the CPMG is significantly higher than that of the *Stage 2* qualifiers which clearly exhibit better image formation under B_1 errors.

In *Stage 3* screening, the four *Stage 2* qualifiers were evaluated under alternating B_1 errors. These four variants all performed similarly, with the exception of the location of spike artifact in the reconstructed image. As shown in Table 4, the variance (σ^2) for variants S011[90, −90, 90, −90] and S012[−90, 90, −90, 90] are higher in scan 2, i.e. when the object was placed at the edge of the FOV. The reason for this behaviour was the presence of the spike (artifact) at the center of the FOV when the object was placed near the edge. Variants S007[90, 0, 90, 0] and S015 [−90, 180, −90, 180] also generated similar spike artifacts but at the very edge of the FOV when the object was placed at the center. In this study, variants that generate the largest possible usable FOV were of interest. To avoid artifacts at the center of the FOV

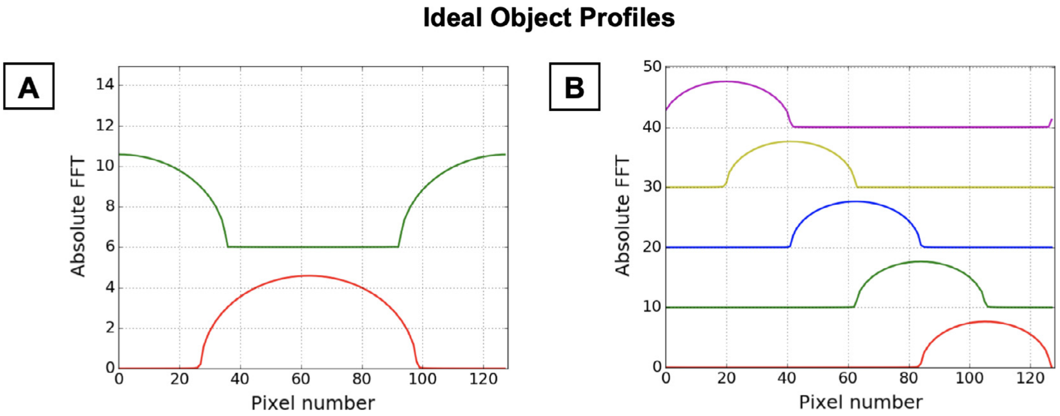

Fig. 3. Reconstructed object profiles under a perfect B_1 field *(i.e. flip angle*$\alpha^J_n = 180^\circ$*)* for TRASE 1D simulation parameters $G_A = +1^\circ$/mm and $G_B = -1^\circ$/mm (90 mm theoretical FOV). (A) 1D profiles of a 50 mm diameter circular object at *Stage 1* simulations i.e. 2 scans with object placed at the center (red plot - scan 1) and the edge (green plot - scan 2) of the FOV. For a perfect flip angle, *Stage 1* results here are equivalent to *Stage 3* results (there will be no alternating B_1 errors for a perfect B_1 field). (B) 1D profiles of a smaller 30 mm diameter circular object at *Stage 2* (i.e. 5 scans with object placed at 5 locations covering the FOV where each plot is shown in a different colour). These ideal profiles were used as a reference to evaluate the performance of 1D TRASE sequences under flip angle errors (B_1 inhomogeneity). The 90 mm FOV seen in Fig. 2 corresponds to 128 pixels (from 128 echoes) for the profiles shown here. *(Profiles from individual scans are vertically shifted to enable visual comparison.)*. (For interpretation of the references to color in this figure legend, the reader is referred to the web version of this article.)

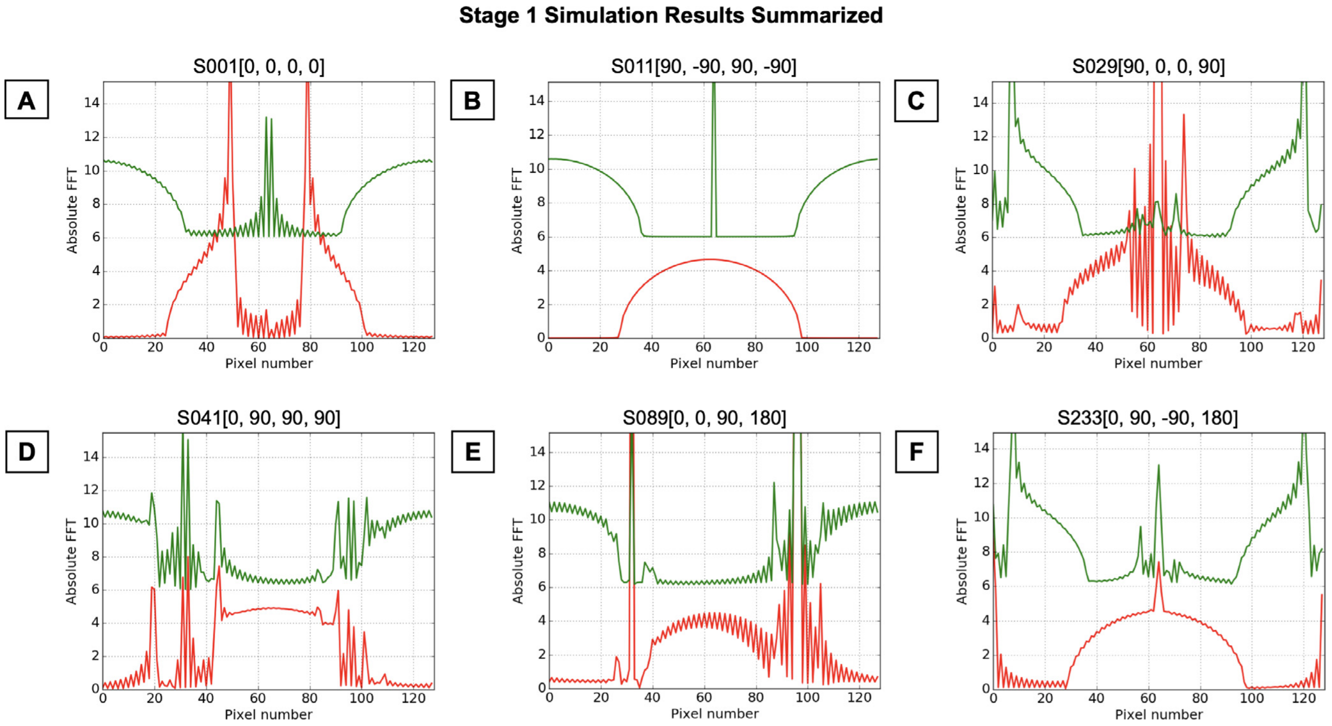

Fig. 4. A summary of the results from *Stage 1* screening simulations *(i.e. 2 scans simulated with imperfect refocusing pulse flip angle* $\alpha_n^J = 160^\circ$*)* showing reconstructed 1D profiles of a 50 mm diameter circular object when placed at the center (red plot – scan 1) and the edge (green plot – scan 2) of the FOV for the sequences (A) S001[0, 0, 0, 0], the CP [11] sequence in super-group 1, sub-group 1 (B) S011[90, −90, 90, −90] in super-group 2, sub-group 2 (C) S029[90, 0, 0, 90] in super-group 3, sub-group 4 (D) S041 [0, 90, 90, 90] in super-group 4, sub-group 5 (E) S089[0, 0, 90, 180] in super-group 5, sub-group 9 and (F) S233[0, 90, −90, 180] in super-group 6, sub-group 15. The division of sequences into super-groups and sub-groups is described in Table 1. (For interpretation of the references to color in this figure legend, the reader is referred to the web version of this article.)

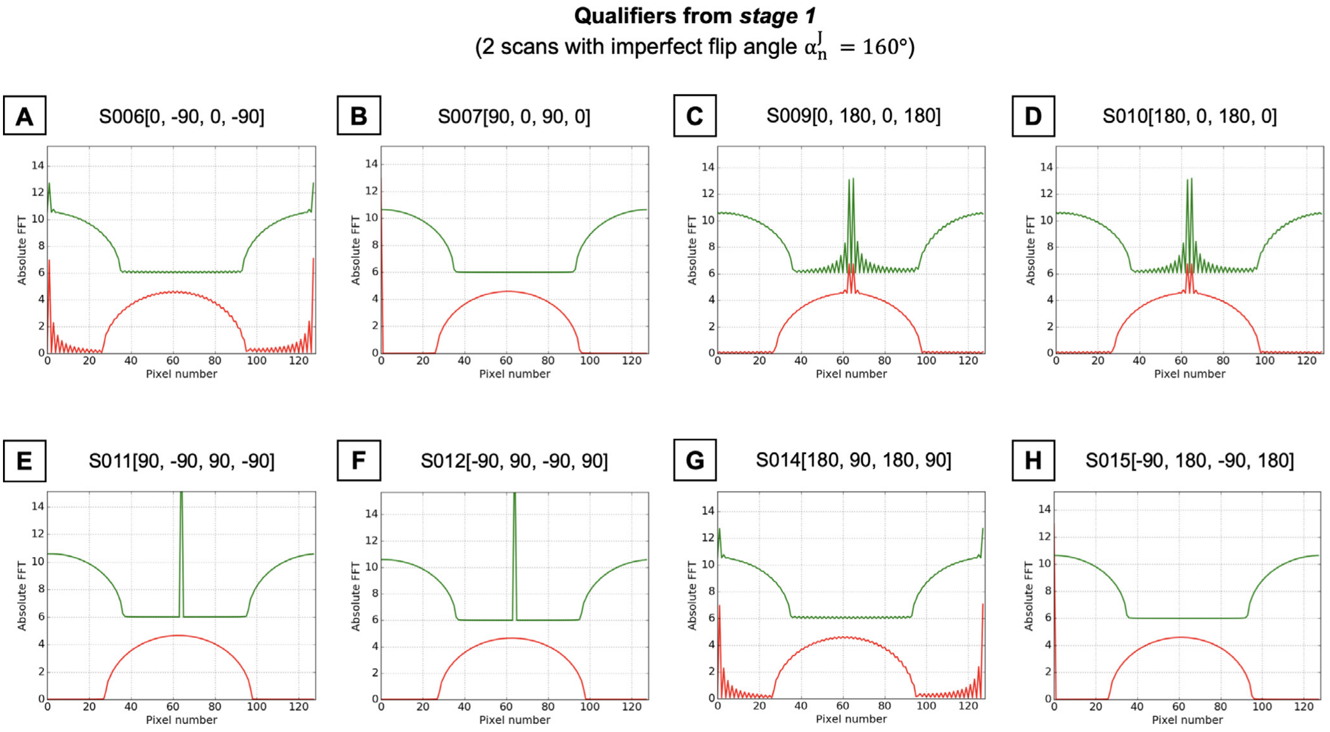

Fig. 5. Results for the 8 variants, belonging to super-group 2, sub-group 2, that passed the *Stage 1* screening *(i.e. 2 scans simulated with imperfect refocusing pulse flip angle* $\alpha_n^J = 160^\circ$*)* showing reconstructed 1D profiles of a 50 mm circular object when placed at the center (red plot – scan 1) and the edge (green plot – scan 2) of the FOV for the sequences (A) S006[0, −90, 0, −90] (B) S007[90, 0, 90, 0] the XY-4 [12] sequence (C) S009[0, 180, 0, 180] (D) S010[180, 0, 180, 0] (E) S011[90, −90, 90, −90] (F) S012 [−90, 90, −90, 90] (G) S014[180, 90, 180, 90] and (H) S015[−90, 180, −90, 180]. (For interpretation of the references to color in this figure legend, the reader is referred to the web version of this article.)

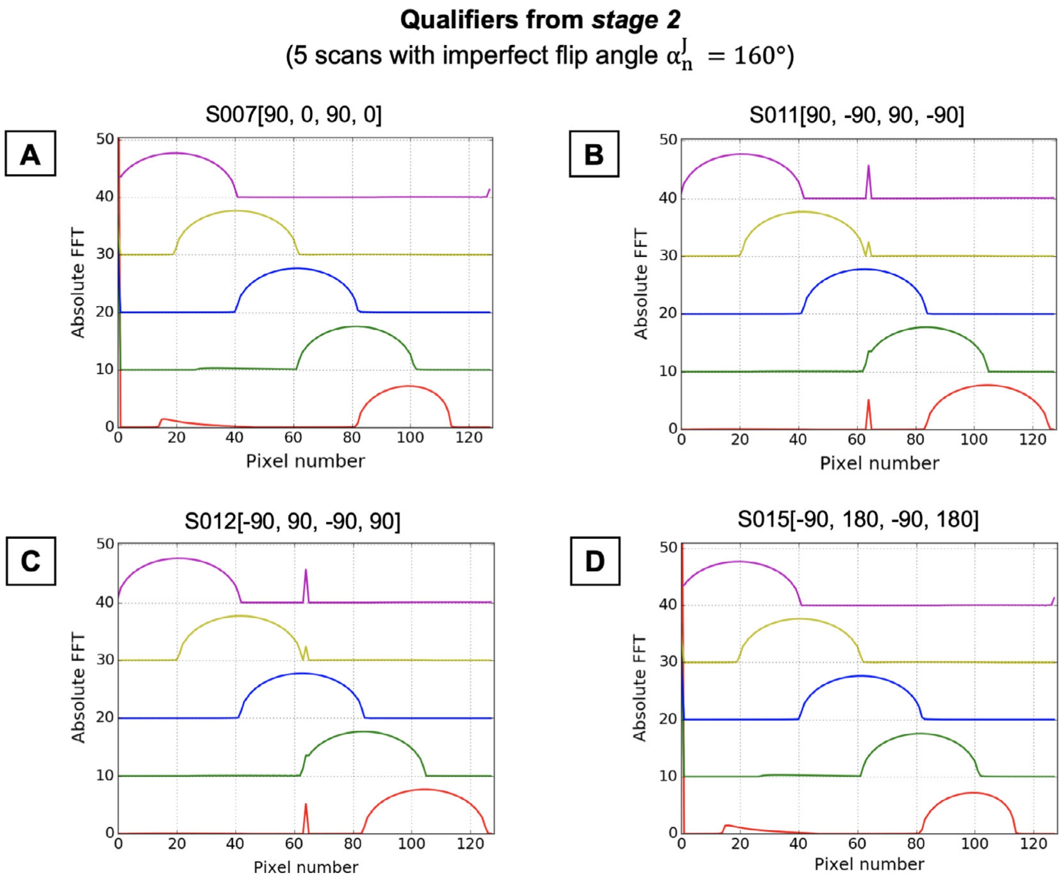

Fig. 6. Results for the 4 variants belonging to super-group 2, sub-group 2 that passed the *Stage 2* screening simulations *(i.e. 5 scans simulated with imperfect refocusing pulse flip angle* $\alpha_n^J = 160^\circ$*)* showing reconstructed 1D profiles for a 30 mm circular object when placed at five locations *(each scan shown in a different colour)* covering the FOV for the sequences (A) S007[90, 0, 90, 0] the XY-4 [12] sequence (B) S011[90, −90, 90, −90] (C) S012[−90, 90, −90, 90] and (D) S015[−90, 180, −90, 180]. (For interpretation of the references to color in this figure legend, the reader is referred to the web version of this article.)

Table 3
List of variants that passed *Stage 2* screening (i.e. 5 scans simulated with imperfect flip angle $\alpha_n^J = 160^\circ$). With $\phi_0 = 0^\circ, \phi_n$ denotes the n^{th} refocusing pulse phase down the echo train. Fields $B_{1,A}(x)_n$ and $B_{1,B}(x)_n$ represent the phases seen by the spins when B_1 phase gradients are applied from coils A and B respectively. $G_J \cdot x$ represents the spatially dependent B_1 phase in degrees for coil J *(for the 1D study here,* $\vec{G_J} \cdot \vec{r} = \vec{G_J} \cdot x\vec{i} = G_J \cdot x$*)*.

SXXX	ϕ_1	ϕ_2	ϕ_3	ϕ_4	$B_{1,A}(x)_n$ Phase n = {1, 3, 5, . . ., N − 1}	$B_{1,B}(x)_n$ Phase n = {2, 4, 6, . . . , N}
S007	90	0	90	0	$G_A \cdot x + 90$	$G_B \cdot x + 0$
S011	90	−90	90	−90	$G_A \cdot x + 90$	$G_B \cdot x - 90$
S012	−90	90	−90	90	$G_A \cdot x - 90$	$G_B \cdot x + 90$
S015	−90	180	−90	180	$G_A \cdot x - 90$	$G_B \cdot x + 180$

Table 4
Stage 1 results of the *Stage 2* qualifiers in comparison with CPMG S002[90, 90, 90, 90]. The usable FOV (as a percentage of the theoretical FOV) was determined from visual inspections of artifacts in *Stage 1* profiles and the σ^2 values represent the variance of 1D image profiles for $\Delta|B_1| = 11\%$ (flip angle 160°) from their ideal profiles (flip angle 180°). *Scan 1: object at the center of the FOV. Scan 2: object at the edges of the FOV.*

Sequence	B_1 Phases	Usable FOV	σ^2 (Scan 1)	σ^2 (Scan 2)
S002	[90, 90, 90, 90]	~ 75%	144.404	1.567
S007	[90, 0, 90, 0]	~ 90%	1.393	0.007
S011	[90, −90, 90, −90]	~ 85%	0.007	1.567
S012	[−90, 90, −90, 90]	~ 85%	0.007	1.567
S015	[−90, 180, −90, 180]	~ 90%	1.393	0.007

in MRI experiments, variants S007[90, 0, 90, 0] and S015 [−90, 180, −90, 180] passed the *Stage 3* screening (see Fig. 7). The S007 (XY-4) and S015 variants were observed to perform identically to each other, which is explicable since S015 and S007 are related by a 180 degree rotation in the transverse plane. Consequently, one of the two variants, S007 (XY-4) first introduced by Maudsley [12], was picked for further PSF-based evaluation.

Fig. 8 demonstrates a comparison of the reconstructed object profiles between the CPMG (S002[90, 90, 90, 90]) and the best-screened XY-4 (S007[90, 0, 90, 0]). From visual examination of

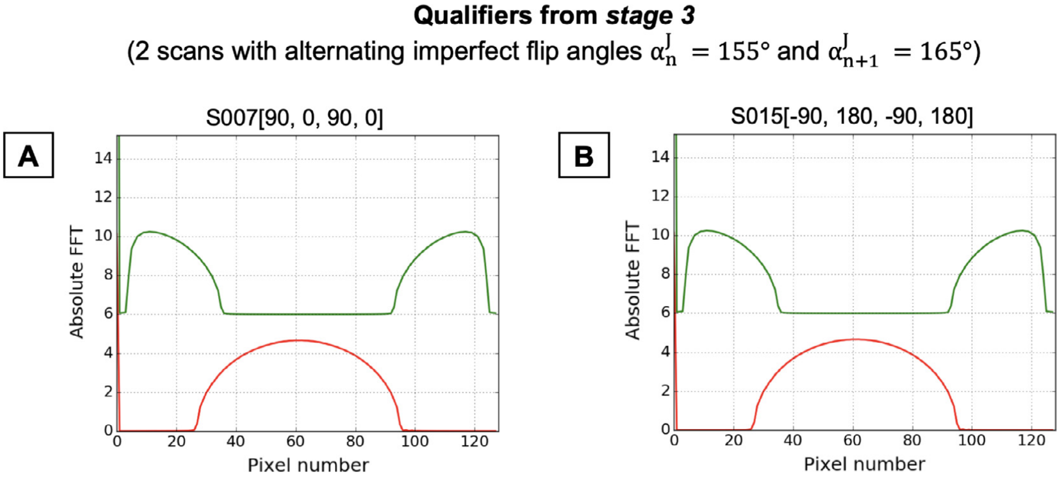

Fig. 7. Results for the 2 variants belonging to super-group 2, sub-group 2, that passed the *Stage 3* of screening simulations *(i.e. 2 scans simulated with alternating flip angles*$\alpha_n^A = 155^\circ$*and*$\alpha_{n+1}^B = 165^\circ$*as in Eq.(9))*. Reconstructed 1D profiles for a 50 mm diameter circular object placed at the center (red plot – scan 1) and the edge (green plot – scan 2) of the FOV are shown for the sequences (A) S007[90, 0, 90, 0] the XY-4 [12] sequence and (B) S015[−90, 180, −90, 180]. These figures also show that responses of the two sequences are identical since they are related by a rotation of 180° about the z axis. The introduction of alternating B_1 errors amplifies the effect of B_1 inhomogeneity and deteriorates image formation at the edges of the FOV as seen in scan 2 *(green)* plots here *(as compared to panels (B) and (H) in*Fig. 5*)*. (For interpretation of the references to color in this figure legend, the reader is referred to the web version of this article.)

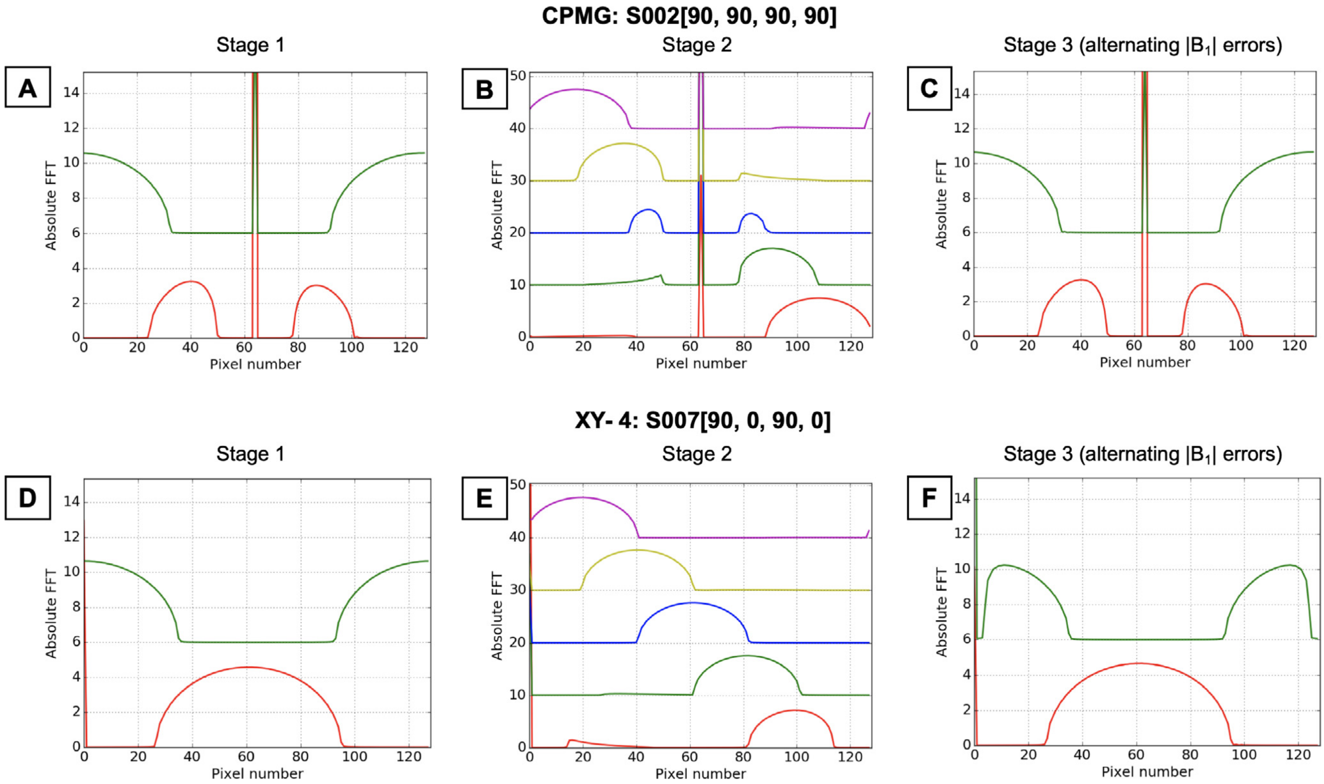

Fig. 8. Screening results – CPMG vs. XY-4: Reconstructed object profiles are shown for CPMG in (A) *Stage 1* i.e. 2 scans with flip angle $\alpha_n^J = 160^\circ$ (B) *Stage 2* i.e. 5 scans with flip angle $\alpha_n^J = 160^\circ$ (C) *Stage 3* i.e. 2 scans with alternating flip angles $\alpha_n^A = 155^\circ, \alpha_{n+1}^B = 165^\circ$ and similarly for XY-4 in (D) *Stage 1* (E) *Stage 2* (F) *Stage 3*. Here, panels (A), (B), and (C) show that CPMG generates a huge spike artifact *(cut-off to enable visibility of object profiles)*. CPMG also exhibits a complete loss in signal at the center with negligible image formation and leaves a significant portion of the FOV unusable. In comparison, XY-4 displays significantly accurate image reconstruction with some artifacts only at one edge of the FOV. See panels (D), (E), and (F) for XY-4 showing a spike artifact at the left edge of the FOV. Panel (E) shows only 1 *(red plot)* out of the 5 scans with a mirrored artifact near the spike and panel (F) shows minimal loss in signal at the edges of the FOV *(scan 2 – green plot)* under alternating B_1 errors. (For interpretation of the references to color in this figure legend, the reader is referred to the web version of this article.)

the 1D profiles it can be seen that XY-4 provides a more accurate image reconstruction while CPMG demonstrates a huge dc spike (artifact) with a poor region of reconstruction at the center the FOV.

4.2. Point Spread Function (PSF) simulations

The point-spread-function (PSF) plots, corresponding to the simulated 90 mm FOV, shown in Fig. 9 demonstrate that PSF is a

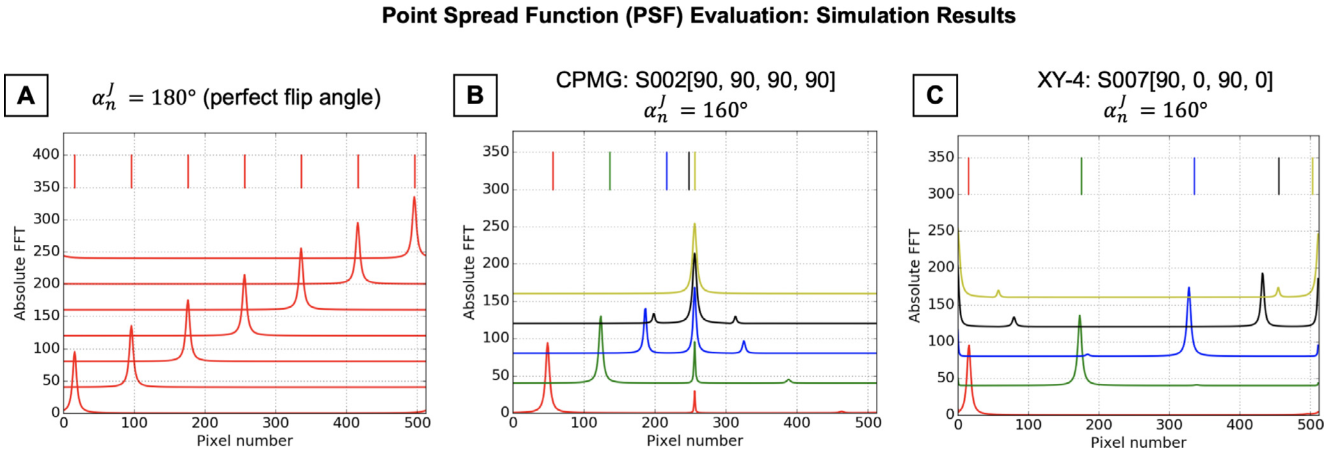

Fig. 9. PSF results for (A) perfect flip angle $\alpha_n^J = 180^\circ$, (B) CPMG with $\alpha_n^J = 160^\circ$, and (C) XY-4 with $\alpha_n^J = 160^\circ$. All PSF plots here have been colour matched with bars that correspond to the position of the point object. Compared to the ideal PSFs (panel A), CPMG in panel B, displays the same spike artifact observed in Fig. 8 which becomes increasingly prominent as the object moves closer to the center of the FOV. The main PSF peaks within close proximity to the spike also deteriorate and generate pairs of mirrored peak artifacts *(see blue and black plots, panel B)*. This loss of PSF peaks in CPMG dominates the center of the FOV and renders a significant portion unusable for TRASE imaging. The PSFs for CPMG are shown for one half of the FOV only to allow visibility of artifacts. However, XY-4 in panel C, displays a larger portion of FOV with good PSF performance and generates a spike artifact along with loss in PSF peaks at one edge of the FOV only (see yellow plot). Moreover, it can be observed that the ideal PSF peaks (panel A) exactly match the object locations whereas the B_1 errors (panels B and C) produce PSFs that are shifted away from the object location. This shift in imperfect PSFs also increases as the object moves closer to the spike artifact. *(Individual plots are vertically shifted to enable visual comparison.)* (For interpretation of the references to color in this figure legend, the reader is referred to the web version of this article.)

function of spatial position for a TRASE MRI experiment. This PSF evaluation closely relates spatial locations with TRASE response and allows for detailed analysis of sequence performance. Fig. 9A shows the PSFs for ideal flip angle $\alpha_n^J = 180^\circ$ which represents a perfectly homogeneous $|B_1|$ field while Fig. 9B and C display the PSFs of CPMG and XY-4 respectively for imperfect flip angle $\alpha_n^J = 160^\circ$.

4.3. Experiments

Fig. 10 shows results from TRASE 1D simulations (with experimental parameters) and experiments for CPMG and XY-4. As observed in the simulations (Figs. 8 and 9), experimental data also demonstrate that XY-4 provides a more accurate reconstruction of the object as compared to CPMG. This confirmation of the simulation results provides ground for further analysis into the TRASE behaviour of sequences studied and understanding of artifacts. However, there were some artifacts observed in the reconstructed object profiles of experimental data which did not show up in simulations. These additional artifacts may be attributed to factors not considered in simulations such as B_0 inhomogeneity and relaxation effects.

5. Discussion

The 256 TRASE sequence variants studied exhibited a wide range of performance, and the fact that only 8 variants passed the *Stage 1* screening emphasizes the importance of selecting an optimum pulse phase scheme. The phases of sequence pairs related by a simple rotation about the z-axis exhibit identical behaviours. Examples of such sequence pairs are: S007 & S015 (Fig. 7), and also S006 & S014, S009 & S010, and S011 & S012 (Fig. 5)). XY-4 exhibits a large percentage ($\sim 90\%$ of the theoretical Nyquist FOV) of usable region within the simulated ($\pm 11\%$) $|B_1|$ inhomogeneity. Both the simulation and experimental data indicate that no other sequence has this level of performance, therefore XY-4 sequence is the best candidate for 1D TRASE imaging using practical transmit coil designs.

It is possible to explain much of the observed simulation behaviour by considering the CP and CPMG sequences. The CP and CPMG sequences are closely related, since for both sequences all the refocusing pulses have identical phases. A series of identical phase pulses preserves the M_y transverse component very well, even for significant amplitude deviations of the B_1 field (CPMG behaviour). The same series of refocusing pulses however causes oscillation between M_x and longitudinal magnetization (M_z), down the echo train (CP behaviour). So, with CP sequences even small errors are rapidly magnified.

Either of the two CP and CPMG behaviours is not conducive to TRASE encoding, which requires that both components of the transverse magnetization (M_x and M_y) be compensated for B_1 errors, so that the transverse phase used to encode spatial information is preserved and allowed to evolve down the echo train. Spatial locations experiencing (substantially) identical refocusing pulse phases in TRASE will in general exhibit both the CP and CPMG behaviours. Any M_y component generated will be preserved (CPMG) and will appear as a dc spike in the TRASE image (FFT spectrum of re-ordered echo train), whereas the amplitude oscillation of the M_x component will appear as a pair of mirrored peak artifacts. Our simulations showed that these two features (spike, mirrored peaks) dominate a significant width of the image in the vicinity of the location experiencing a series of identical phase pulses. No image formation takes place here and there is also the formation of a 'dead region' (of no signal) in between the mirrored peaks.

In the presence of B_1 errors, Maudsley's XY-4 sequence preserves both components of transverse magnetization (M_x and M_y) [12], and therefore also preserves M_z[13]. This is more promising for TRASE, as of course then phase is also preserved. The simulations showed that this favourable behaviour also extends over a large region of the FOV, only finally failing when the condition discussed above (identical refocusing phases) occurs at one end of the FOV, see Fig. 11.

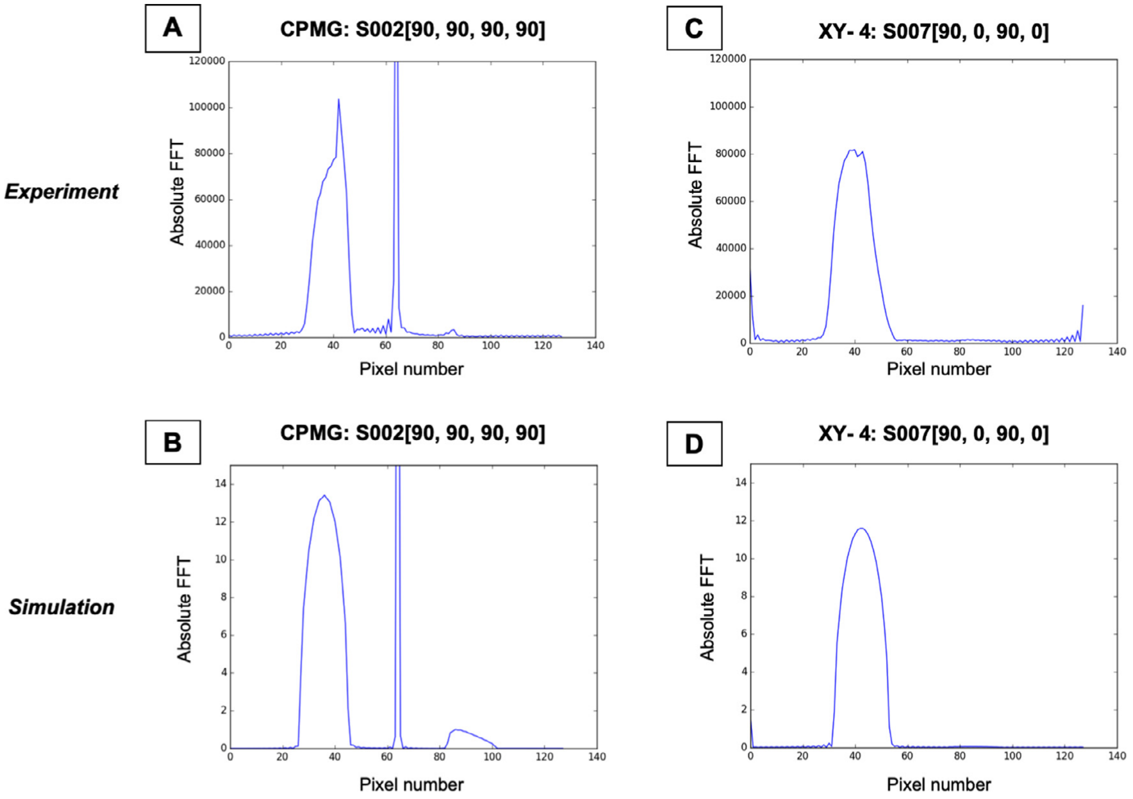

Fig. 10. TRASE 1D experimental results along with equivalent simulations showing reconstructed 1D profiles of a 50 mm diameter cylindrical object using CPMG for both (A) Experiment, (B) Simulation; and using XY-4 for both (C) Experiment, (D) Simulation. The experiments were conducted on a 0.2T MRI using a cylindrical bottle (~50 mm diameter) containing salt water. Both experimental and simulation procedures here collected 128 echoes and used pulse sequences consisting of 200 µs pulses with an echo spacing of 900 µs. The simulations however were performed under alternating B_1 errors (flip angles $\alpha_n^A = 165^\circ$ and $\alpha_{n+1}^B = 170^\circ$) to account for calibration errors between two real transmit coils. The spike artifact in CPMG (panels A and B) has been cut-off for visibility of the profiles. The same reconstruction code was used for experimental and simulation data to allow unbiased interpretation of results. These results re-emphasize the performance of XY-4 vs. CPMG (as described in Figs. 8 and 9) and demonstrate that experimental data substantially match simulations.

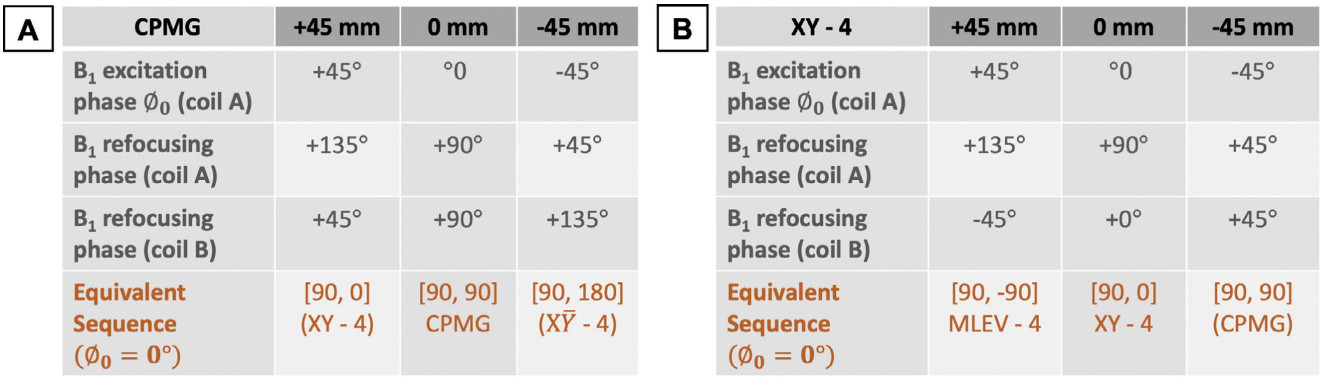

A

CPMG	+45 mm	0 mm	-45 mm
B_1 excitation phase $\emptyset_0$ (coil A)	+45°	°0	-45°
B_1 refocusing phase (coil A)	+135°	+90°	+45°
B_1 refocusing phase (coil B)	+45°	+90°	+135°
Equivalent Sequence ($\emptyset_0 = 0°$)	[90, 0] (XY - 4)	[90, 90] CPMG	[90, 180] ($X\bar{Y}$ - 4)

B

XY - 4	+45 mm	0 mm	-45 mm
B_1 excitation phase $\emptyset_0$ (coil A)	+45°	°0	-45°
B_1 refocusing phase (coil A)	+135°	+90°	+45°
B_1 refocusing phase (coil B)	-45°	+0°	+45°
Equivalent Sequence ($\emptyset_0 = 0°$)	[90, -90] MLEV - 4	[90, 0] XY - 4	[90, 90] (CPMG)

Fig. 11. An explanation of artifacts in 1D TRASE for (A) CPMG [90, 90, 90, 90] and (B) XY-4 [90, 0, 90, 0] using a TRASE gradient pair of $G_A = +1^\circ$/mm and $G_B = -1^\circ$/mm (FOV = 90 mm). The poor performance of CPMG at 0 mm is explained in the main text. It can be seen that the field phases for XY-4 (−45 mm) are simply a global −45° shift relative to CPMG (0 mm), explaining the poor performance of XY-4 TRASE at this location which corresponds to the loss in PSF peaks at one edge of the FOV (see panel C Fig. 9). Conversely, CPMG at both $x = -45$ mm and +45 mm and XY-4 at +45 mm all experience variants of XY-4 which compensate for all components of magnetization M and thus perform well for TRASE. The main observation is that by selecting optimum B_1 transmit pulse phases (XY-4), the artifact-generating condition of identical refocusing phases occurs at one edge of the FOV only, where they can be conveniently avoided.

6. Conclusion

An exhaustive study of 256 TRASE sequences was performed, considering all combinations of echo train RF pulse phases, for repeating patterns of groups of 4 phases, with phases selected from the set: 0, −90, +90, 180 degrees. We considered on-resonance behaviour only. From this study, Maudsley's XY-4 sequence (our S007[90, 0, 90, 0]) exhibits the least sensitivity to B_1 inhomogeneity in TRASE. We conclude that B_1 errors causing a flip angle range between 160° and 200° ($\Delta|B_1| = \pm 11\%$) are acceptable. Under these design constraints, the usable FOV for XY-4 is ~ 90% of the maximum possible FOV, representing a practically acceptable performance and an improvement over previously used TRASE sequences. These results will be useful in phase gradient RF coil design, for which B_1 inhomogeneity is an important design parameter. This study illustrates how sequence design, coil design and flip angle calibration are inter-related. Future directions include extension to more complex 2D TRASE sequences.

Acknowledgements

Natural Sciences and Engineering Research Council of Canada (NSERC) Discovery grants to GES and JCS (RGPIN-2016-05183), and Canadian Space Agency (CSA) FAST grant to GES.

References

[1] Jonathan C. Sharp, Scott B. King, MRI using radiofrequency magnetic field phase gradients, Magn. Reson. Med. 63 (1) (2010) 151–161.

[2] Gordon E. Sarty, Andre Obenaus, Magnetic resonance imaging of astronauts on the international space station and into the solar system, Can. Aeronaut. Space J. 58 (1) (2012) 60–68.

[3] Gordon E. Sarty et al., A magnetic resonance imager for the international space station, in: International Astronautical Federation, 63rd International Astronautical Congress, Naples, Italy, 2012.

[4] Gordon E. Sarty et al., Compact MRI for astronaut physiological research and medical diagnosis, in: AIAA SPACE 2012 Conference & Exposition, 2012, p. 5240.

[5] Scott B. King, Jonathan C. Sharp. Method for radio-frequency nuclear magnetic resonance imaging, US Patent 8,159,222, Apr. 2012.

[6] Jonathan C. Sharp, Scott B. King, RF based spatially selective excitation in MRI, US Patent 8,228,062, July 2012.

[7] Jonathan C. Sharp et al., Imaging without gradients: first in vivo MR images using the TRASE RF imaging method, in: Proc. 20th Annu. Meet. Int. Soc. Magn. Res. Med 705, 2012.

[8] Jonathan C. Sharp et al., High-resolution MRI encoding using radiofrequency phase gradients, NMR Biomed. 26 (11) (2013) 1602–1607.

[9] Erwin L. Hahn, Spin echoes, Phys. Rev. 80 (4) (1950) 580.

[10] Saul Meiboom, David Gill, Modified spin-echo method for measuring nuclear relaxation times, Rev. Sci. Instrum. 29 (8) (1958) 688–691.

[11] Herman Y. Carr, Edward M. Purcell, Effects of diffusion on free precession in nuclear magnetic resonance experiments, Phys. Rev. 94 (3) (1954) 630.

[12] A.A. Maudsley, Modified Carr-Purcell-Meiboom-Gill sequence for NMR fourier imaging applications, J. Magn. Reson. (1969) 69 (3) (1986) 488–491.

[13] Terry Gullion, David B. Baker, Mark S. Conradi, New, compensated Carr-Purcell sequences, J. Magn. Reson. (1969) 89 (3) (1990) 479–484.

[14] Malcolm H. Levitt, Ray Freeman, Thomas Frenkiel, Broadband decoupling in high-resolution nuclear magnetic resonance spectroscopy, Advances in Magnetic and Optical Resonance, vol. 11, Elsevier, 1983, pp. 47–110.

[15] A.J. Shaka, S.P. Rucker, A.N.D.A. Pines, Iterative Carr-Purcell trains, J. Magn. Reson. (1969) 11 (3) (1988) 606–611.

[16] B.J. Suh, F. Borsa, D.R. Torgeson, Use of an alternating-phase CPMG sequence to avoid spin-locking effects inT2 measurements in solids, J. Magn. Reson. Ser. A 110 (1) (1994) 58–61.

[17] F. Balibanu et al., Nuclear magnetic resonance in inhomogeneous magnetic fields, J. Magn. Reson. 145 (2) (2000) 246–258.

[18] Somaie Salajeghe, Paul Babyn, Gordon E. Sarty, Composite pulses for RF phase encoded MRI: a simulation study, Magn. Reson. Imag. 36 (2017) 40–48.

[19] Jason P. Stockmann et al., Transmit Array Spatial Encoding (TRASE) using broadband WURST pulses for RF spatial encoding in inhomogeneous B 0 fields, J. Magn. Reson. 268 (2016) 36–48.

[20] Felix Bloch, Nuclear induction, Phys. Rev. 70 (7-8) (1946) 460.

[21] Hongwei Sun, Stephanie Yong, Jonathan C. Sharp, The twisted solenoid RF phase gradient transmit coil for TRASE imaging, J. Magn. Reson. 299 (2019) 135–150.